Geophysical Journal International

Geophys. J. Int. (2010) **182,** 1013–1024 doi: 10.1111/j.1365-246X.2010.04662.x

Radial anisotropy along the Tethyan margin

Sung-Joon Chang,[1] Suzan van der Lee,[1] Eric Matzel[2] and Heather Bedle[1,*]

[1] *Department of Earth and Planetary Sciences, Northwestern University,* 1850 *Campus Drive, Evanston,* IL 60208-2150, *USA.* *E-mail: sjchang@earth.northwestern.edu*

[2] *Lawrence Livermore National Laboratory,* PO Box 808, L-205, *Livermore, CA* 94551, *USA*

Accepted 2010 May 13. Received 2010 May 12; in original form 2010 March 15

SUMMARY

We estimate radial anisotropy along the Tethyan margin by jointly fitting regional *S* and Love waveform trains and fundamental-mode Love-wave group velocities. About 3600 wave trains with *S* and Love waves and 5700 Love-wave group velocity dispersion curves are jointly inverted for *SH*-velocity perturbations from a pre-existing, 3-D *SV*-velocity model. These perturbations are predominantly positive (*SH* faster than *SV*) and consistent with PREM, but our model also shows significant lateral variation in radial anisotropy that appears to be correlated with tectonic environment. *SH* waves travel faster than *SV* wave beneath backarc basins, oceans and orogenic belts such as the Tyrrhenian and Pannonian basins, the Ionian Sea, the Alps, the Apennines, the Dinarides and the Caucasus. The Algero-Provençal basin, however, is underlain by faster *SV* velocity. Faster *SV* velocity of radial anisotropy is also detected within cratons such as the East European platform and the Arabian shield. Beneath hotspots we detect a change in radial anisotropic polarity with depth, which may be caused by transition between the lattice-preferred orientation from horizontal deformation in the asthenosphere and the shape-preferred orientation from vertically oriented melt channels in the lithosphere. We also find significant portion of radial anisotropy within subducting slabs depends on the slab's dip angle.

Keywords: Body waves; Surface waves and free oscillations; Seismic anisotropy; Seismic tomography; Asia; Europe.

1 INTRODUCTION

The uppermost mantle is widely observed to have significant seismic anisotropy (Dziewoński & Anderson 1981; Silver 1996; Panning & Romanowicz 2006), which is generally thought to be caused by the lattice preferred orientation (LPO) of dominant upper mantle minerals, olivine and pyroxene (Estey & Douglas 1986). LPO is related to strain by tectonic stress or asthenospheric flow, and so seismic anisotropy can characterize traces of past tectonics or current mantle flow in the Earth, implying the evolution of tectonic regimes and mantle convection.

Much of the research into the Earth's anisotropy has been focused on azimuthal anisotropy from shear wave splitting (e.g. Silver & Chan 1991; Silver 1996; Savage 1999), including studies that focused on a significant part of the Tethyan margin (Schmid *et al.* 2004; Lucente *et al.* 2006). Other studies have concentrated on estimating radial anisotropy, globally (Montagner & Tanimoto 1991; Ekström & Dziewoński 1998; Plomerová *et al.* 2002; Gung *et al.* 2003; Panning & Romanowicz 2006) and on smaller, continental scales (e.g. Marone *et al.* 2004a; Sebai *et al.* 2006; Marone *et al.* 2007). Radial anisotropy provides information on mantle dynamics because the direction of mantle flow, water or melt content and mantle rheology determine the orientation of fast *S*-velocity axes. Mantle flow can result in different orientation of fast *S*-velocity axes. For example, in case of normal dry olivine, horizontal mantle flows induce faster *SH* velocity, while vertical flows result in faster *SV* velocity (Karato *et al.* 2008).

We estimate radial anisotropy along the Tethyan margin which includes Europe, the Mediterranean Sea, northern Africa, the Middle East and central Asia. Tectonic features in the study area are indicated in Fig. 1. Chang *et al.* (2010) estimated a 3-D *SV*-velocity model for this region by jointly inverting teleseismic *S* and *SKS* arrival times, regional *S* and Rayleigh waveform fits, fundamental-mode Rayleigh-wave group velocities and independent Moho depth constraints. This *SV*-velocity model can also explain part of our *SH* data, but only 28 per cent of misfit variance for *S* and Love wave trains and 38 per cent for Love-wave group velocities. This variance is with respect to wave trains and group velocities predicted by the regional 1-D model MEAN (Marone *et al.* 2004b). We thus inverted our *SH* data, which consists of regional *S* and Love wave trains and fundamental-mode Love-wave group velocities, for radially anisotropic anomalies with respect to the 3-D isotropic

*Now at: Chevron North America Exploration and Production Company, Gulf of Mexico SBU, 100 Northpark Boulevard, Covington, LA 70443, USA.

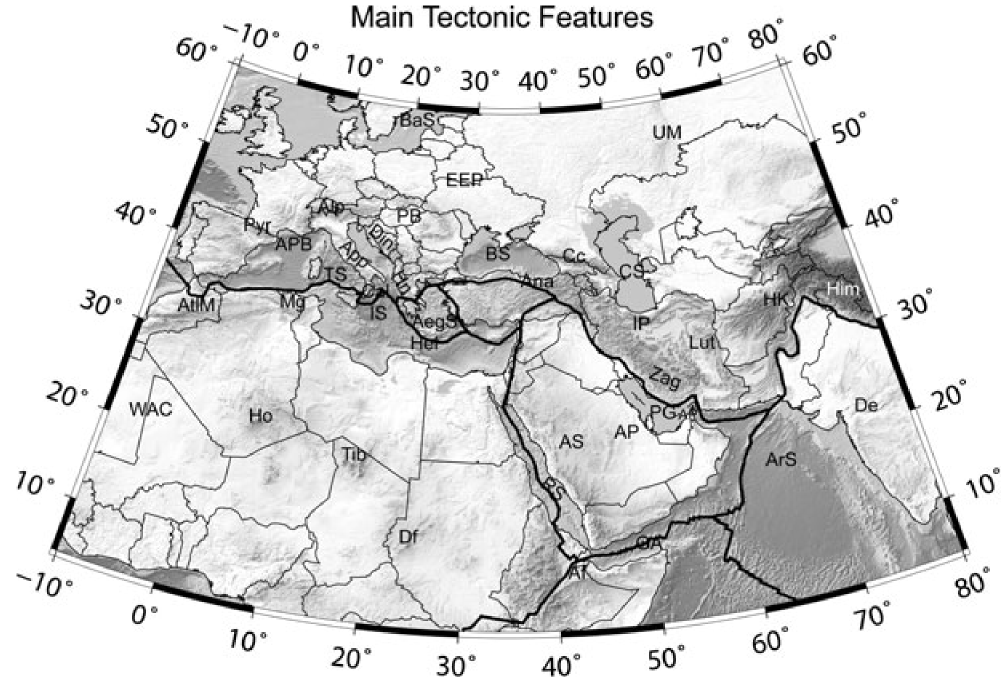

Figure 1. Topographic map and main tectonic features for the Tethyan margin. Thick solid lines indicate plate boundaries, which are from Bird (2003). AegS, Aegean Sea; Af, Afar; Alp, Alps; Ana, Anatolian plateau; AP, Arabian platform; APB, Algero-Provençal basin; ArS, Arabian Sea; AS, Arabian shield; AtlM, Atlas Mts; BaS, Baltic shield; BS, Black Sea; Cal, Calabrian arc; Cc, Caucasus; CS, Caspian Sea; De, Deccan traps; Df, Darfur;Din, Dinarides; EEP, East European platform; GA, Gulf of Aden; Hel, Hellenic arc; Him, Himalayas; HK, Hindu Kush; Hn, Hellenides; Ho, Hoggar; IP, Iranian plateau; IS, Ionian Sea; Lut, Lut block; Mg, Maghrebides; PB, Pannonian basin; PG, Persian Gulf; Pyr, Pyrenees; RS, Red Sea; Tib, Tibesti; TS, Tyrrhenian Sea; UM, Ural Mts; WAC, West African craton; Zag, Zagros belt.

SV-velocity model. In essence we use the 3-D *SV*-velocity model as a reference model for the inversion of our *SH* data for radial anisotropy. We describe the methodology and data sets of the joint inversion and perform resolution tests to investigate the resolving power of the joint inversion. Finally, we apply the joint inversion to observed data sets to produce a radial anisotropic model for the Tethyan margin and interpret characteristics of the estimated radial anisotropy.

2 METHOD

The average *SH* velocity in the uppermost mantle has been observed roughly 0.2 km s^{-1} faster than *SV* velocity beneath both oceanic and continental lithosphere (Hess 1964; Bamford 1973, 1977). Global 1-D model PREM (Dziewoński & Anderson 1981) included such an anisotropic layer to 220 km depth. Interestingly, 3-D models of *SV* and *SH* velocity are remarkably well correlated down to regional scales (Gung *et al.* 2003). This suggests that a 3-D *SV*-velocity model would be an excellent reference model for estimating radial anisotropy, if we consider *SH* velocity deviations from the 3-D *SV* reference model to represent radial anisotropy. In a previous paper (Chang *et al.* 2010), we estimated an *SV*-velocity mantle model for the Tethyan margin by jointly inverting teleseismic *S* and *SKS* arrival times, regional *S* and Rayleigh waveform fits, fundamental-mode Rayleigh-wave group velocities and independent Moho depth constraints. Indeed, this *SV* velocity model explains 30–40 per cent of our *SH* and Love data sets. Here, we use the transverse components of the same data set to resolve the *SH*-velocity structure. We adopted the 3-D *SV*-velocity model as a reference model, and inverted regional *S* and Love waveform fits and fundamental-mode Love-wave group velocity residuals to estimate *SH*-velocity perturbations relative to the 3-D *SV*-velocity model. These imaged *SH*-velocity perturbations are thus a direct, approximation of radial anisotropy.

We use the same model parametrization as used for constructing the *SV*-velocity model of Chang *et al.* (2010). This parametrization includes a set of spherical shells of gridpoints to support the *SH*-velocity distribution at various depths, and the gridpoints are derived through triangular tesselation of a sphere (Baumgardner & Frederickson 1985; Wang & Dahlen 1995). The *SH* velocities are defined through linear interpolation between these grid nodes. The horizontal distance between our gridpoints is ∼100 km on the surface. The centre of our grid is located at 35°N/22.5°E and extends 70° in all directions. Further details may be found in Chang *et al.* (2010).

SH velocities can be estimated by solving the equation,

$$\mathbf{G}_{SH}\mathbf{m}_{SH} = \mathbf{d}_{SH}, \tag{1}$$

where $\mathbf{G}_{SH}$ is the sensitivity kernel of multimode Love-wave data to *SH* velocity, $\mathbf{d}_{SH}$ is the *SH* data vector consisting of waveform fitting constraints and group velocity residuals relative to predictions from 1-D reference model MEAN (Marone *et al.* 2004b), and $\mathbf{m}_{SH}$ are *SH* velocity perturbations relative to the MEAN. In this study, sensitivity kernels vary in the depth dimension and from path to path, but they do not vary along a path. Recasting eq. (1) in terms that includes the 3-D reference *SV*-velocity model gives,

$$\mathbf{d}_{SH} = \mathbf{G}_{SH}\mathbf{m}_{SH} = \mathbf{G}_{SH}(\mathbf{m}_{SV} + \boldsymbol{\Delta\beta}_{SH}) = \mathbf{d}_{VH} + \boldsymbol{\Delta}\mathbf{d}_{SH}, \tag{2}$$

where $\mathbf{m}_{SV}$ represents the 3-D reference *SV*-velocity model relative to the 1-D reference model MEAN, $\boldsymbol{\Delta\beta}_{SH}$ is *SH* velocity perturbation relative to the 3-D *SV* velocity model, and $\mathbf{d}_{VH}$ are the data predicted by $\mathbf{m}_{SV}$ using the Love-wave data coverage and corresponding sensitivity from $\mathbf{G}_{SH}$. Therefore, subtracting $\mathbf{d}_{VH}$ from

$\mathbf{d}_{SH}$, we have the following equation:

$$\mathbf{G}_{SH}\boldsymbol{\Delta\beta}_{SH} = \boldsymbol{\Delta}\mathbf{d}_{SH}. \tag{3}$$

$\mathbf{G}_{SH}$ and $\boldsymbol{\Delta}\mathbf{d}_{SH}$ are represented in detail as follows:

$$\mathbf{G}_{SH} = \begin{bmatrix} w_{rw}\mathbf{A}^{\mathbf{rw}} \\ w_U\mathbf{A}^{\mathbf{U}} \\ w_1\mathbf{I} \\ w_2\mathbf{F_h} \\ w_3\mathbf{F_v} \end{bmatrix} \quad \text{and} \quad \boldsymbol{\Delta}\mathbf{d}_{SH} = \begin{bmatrix} w_{rw}\left(\mathbf{d}_{SH}^{rw} - \mathbf{d}_{VH}^{rw}\right) \\ w_U\left(\mathbf{d}_{SH}^{U} - \mathbf{d}_{VH}^{U}\right) \\ 0 \\ 0 \\ 0 \end{bmatrix}, \tag{4}$$

where $\mathbf{A}^{\mathbf{rw}}$ is a sensitivity kernel matrix that consists of linear constraints along ray paths estimated by partitioned waveform inversion (Nolet 1990; Van der Lee & Nolet 1997). Matrix component, $\mathbf{A}^{\mathbf{U}}$, represents partial derivatives of group velocity with respect to the *SH*-velocity perturbations, and $\mathbf{d}^{\mathrm{rw}}_{\mathrm{phase}}$ and $\mathbf{d}^{\mathrm{U}}_{\mathrm{phase}}$ are data vectors for regional waveform fits and group velocities from $\mathbf{d}_{\mathrm{phase}}$, respectively. To weight each datum according to its quality, we scaled equations associated with each datum by the inverse of the corresponding measurement error (uncertainty). Weights w_{rw} and w_{U} are for data sets of regional waveform fits and group velocities, respectively, and those are used to ensure that each data set obtains significant variance reduction. Components $\mathbf{I}$, $\mathbf{F_h}$ and $\mathbf{F_v}$ represent the damping, horizontal and vertical flattening operators with weights w_i ($i =$ 1, 2, 3), respectively. Flattening operators are differentials between two lateral or vertical contiguous gridpoints (Constable *et al.* 1987; VanDecar 1991).

The *SH*-velocity perturbations, $\boldsymbol{\Delta\beta}_{SH}$, are obtained by solving eq. (3) with the iterative algorithm LSQR (Paige & Saunders 1982a, b) and represent velocity differences between *SH* and *SV* velocities, thereby indicating radial anisotropy.

3 DATA

We fit *S* and Love waveforms from 3584 seismograms, which sample the Mediterranean Sea, Europe, the Middle East, central and southern Asia, northern Africa, the Red Sea and part of the East European platform. For the Mediterranean region, we adopted waveform fit data from Marone *et al.* (2004a). The great-circle wave propagation paths for these seismograms with locations of events and stations are shown in Fig. 2(a). The frequency content of the waveforms generally falls within the range of 0.006 and 0.1 Hz.

Love-wave group velocities were measured on transverse broadband displacement seismograms filtered by a narrow band Gaussian filter centred over many different periods. We use Love-wave group velocities from previous research (Pasyanos & Nyblade 2007). The number of total fundamental-mode Love-wave group–velocity dispersion curves reaches to 5676. The period for group velocities ranges from 7 to 100 s. Data coverage for the group velocity data set is better than that for the waveform fits as shown in Fig. 2(b), because source mechanisms are not required for the measurement of dispersion curves. Our 3-D reference model also includes a laterally varying Moho depth. These Moho depths were constrained by *SV*-velocity data (regional *S* waveform fits and fundamental-mode Rayleigh-wave group velocities) as well as receiver functions, seismic refraction/reflection experiments and gravity surveys (Marone *et al.* 2003; Chang *et al.* 2010).

4 ERROR AND RESOLUTION

4.1 Crustal correction

Crustal correction is essential in surface wave tomography because even long-period surface waves are sensitive to crustal structure (Panning & Romanowicz 2006; Marone & Romanowicz 2007; Bozdağ & Trampert 2008). Therefore, it is not appropriate to approximate the effect of crustal structure with linear correction based on a single reference model. We calculate sensitivity kernels for regional waveforms and fundamental-mode Love-wave group velocities with non-linear crustal correction based on several reference models. A reference model is chosen for each ray path according to average Moho and water layer along the path based on previous research on the study region (Marone *et al.* 2003) or CRUST2.0 (Bassin *et al.* 2000).

Although the *SH* sensitivity kernels include sensitivity to Moho depth, which is needed to predict the effect of the 3-D reference Moho depth on the *SH* data, we do not allow the Moho from our 3-D reference model to change during the inversion of the residual *SH* data.

4.2 Resolution tests

To assess the resolving power of our *SH* data and joint inversion for radial anisotropy, we performed a resolution test with ± 200 m s^{-1} cylindrical anomalies with radii of 3° (Fig. 3). We calculate synthetic data by multiplying the kernel matrices in eq. (4) with the test model and adding Gaussian random noise with a standard deviation in proportion to the estimated uncertainty of our data. Anomalies are well resolved down to 150 km depth, but below 200 km only anomalies beneath the eastern Mediterranean and the Middle East are resolved with amplitudes comparable to the original model. Weights in the joint inversion for *S* and Love waveform fits and Love-wave group velocities are set to 1.6 and 2.0, respectively. After numerous trials in tests, we set these values to recover anomalies well for the uppermost mantle and to allow each data set to achieve significant variance reduction.

To assess vertical resolution of the joint inversion, checkerboard tests are performed for several vertical cross-sections (Fig. 4). All cross-sections generally show good resolution at depths above 120 km, and some sections (B-b and part of D-d and E-e) present fair depth resolution down to 250–300 km. Section A-a appears least well resolved, but the polarity change of radial anisotropy is resolved.

4.3 Errors in methodology

In this study, an *SH* velocity model is estimated based on a predetermined 3-D *SV* velocity model as a reference, and the difference between *SV* and *SH* velocities is interpreted as radial anisotropy. Because *SH* body waves and higher mode Love waves also have sensitivity to *SV* velocity, a joint inversion of *SV*, *SH*, Rayleigh and Love waves for *SV* and *SH* velocities as well as anisotropic parameter $\xi = (\frac{V_{SH}^2}{V_{SV}^2})$ is a theoretically sounder approach to the estimation of radial anisotropy. In practice, however, the error we make by separately inverting *SH* and Love data is very small, because our data set is dominated by fundamental-mode Love waves and regional body waves and higher modes are only included if they have zero sensitivity to the lower mantle structure, thus strongly limiting the distances over which the *SH* wave path are near-vertical.

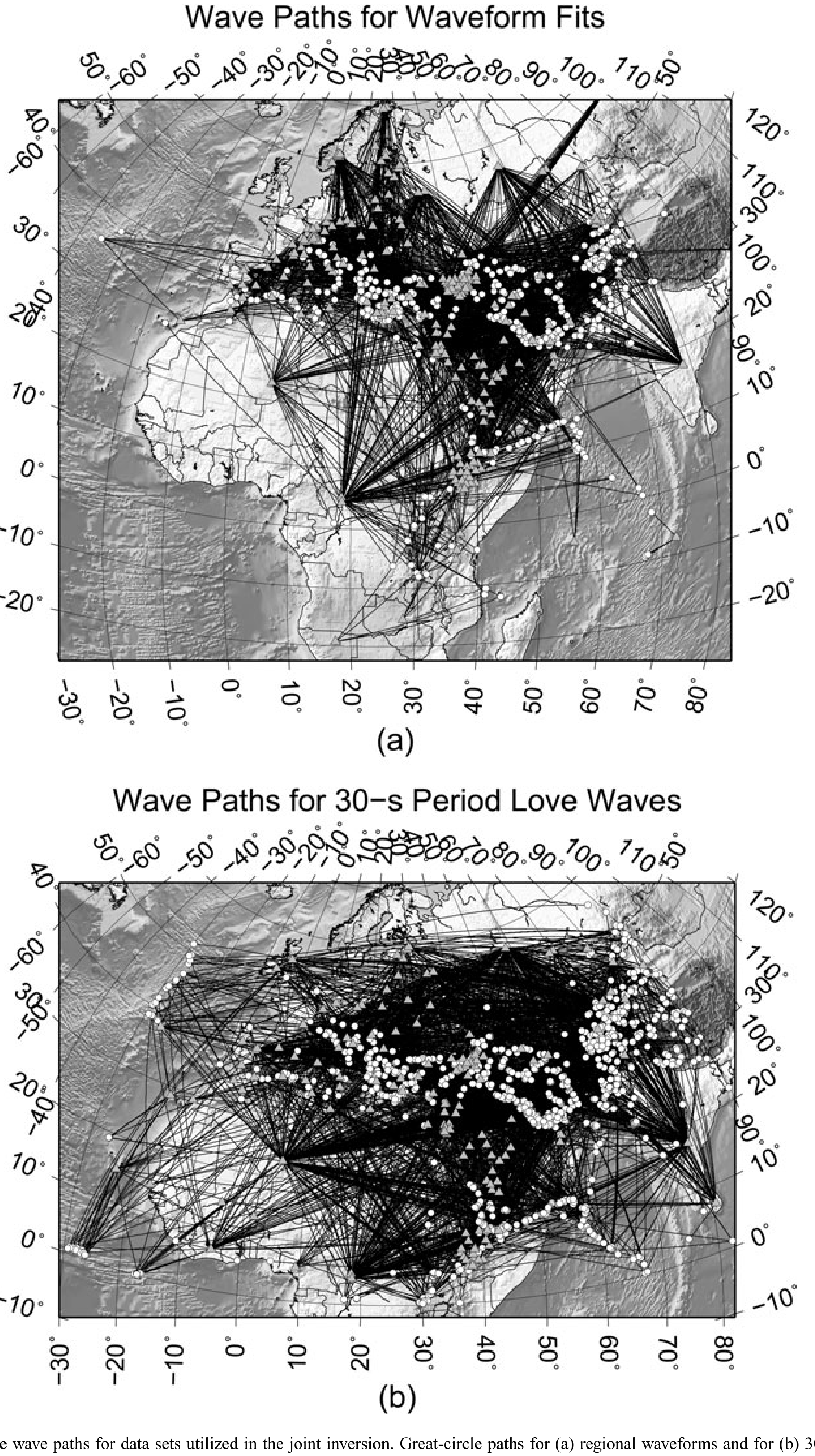

Figure 2. Great-circle wave paths for data sets utilized in the joint inversion. Great-circle paths for (a) regional waveforms and for (b) 30-sec period Love waves are shown in black lines. Events and stations are indicated in white circles and grey triangles, respectively.

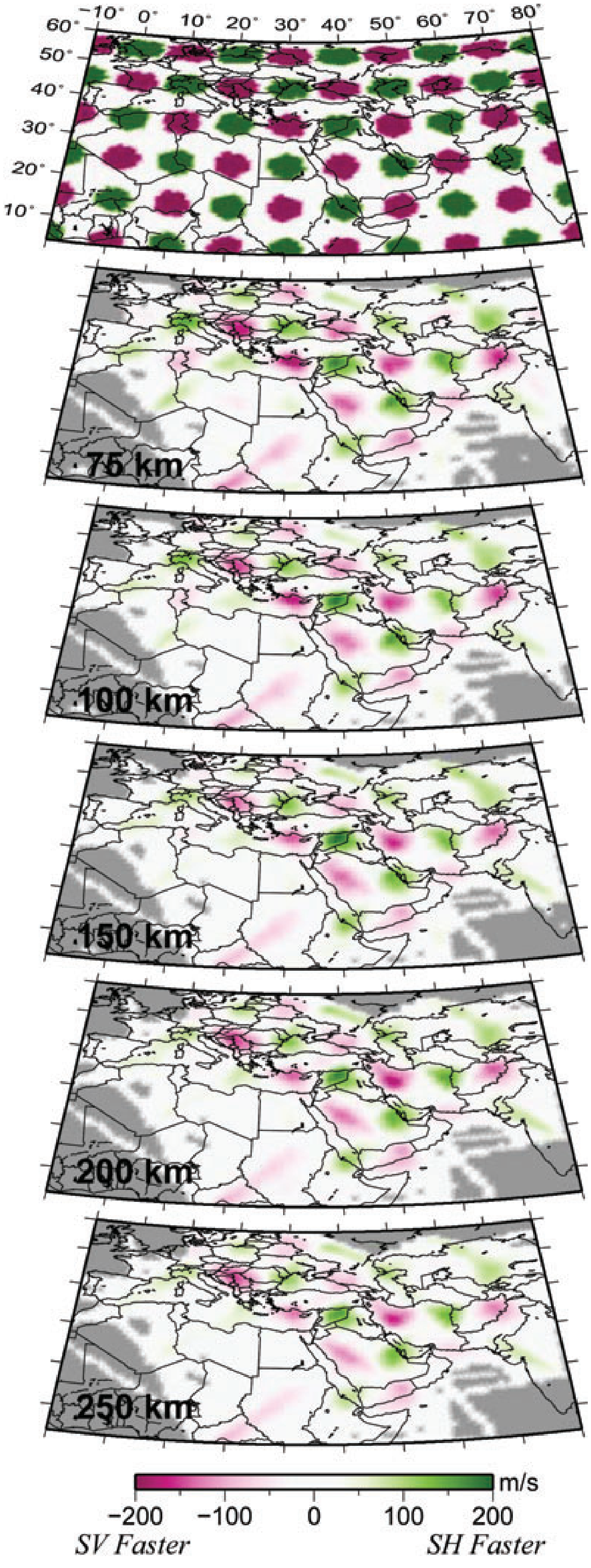

Figure 3. Resolution test results for the joint inversion. True model with $\pm 200\,\mathrm{m\,s^{-1}}$ cylindrical anisotropic anomalies is shown on the top and results at 75, 100, 150, 200 and 250 km depths are shown subsequently. Regions not covered by data set are in grey.

Furthermore, separate inversions for SV and SH velocities give high correlation above 0.9 with simultaneous inversion of isotropic S and anisotropic parameter, ξ, for the upper mantle in Panning & Romanowicz (2006). The result of our inversion is shown in Fig. 5(a).

However, because we have inverted the SH and Love wave data separately, and with different sensitivities, from the SV and Rayleigh data, the possibility exists that our SH velocity model contains an isotropic component that went previously undetected by the SV and Rayleigh data. To remove this undetected isotropic part we divide the anisotropic model $\boldsymbol{\Delta\beta}_{SH}$ into two parts as follows,

$$\boldsymbol{\Delta\beta}_{SH} = \boldsymbol{\Delta\beta}_{SH-i} + \boldsymbol{\Delta\beta}_{SH-a}, \tag{5}$$

where $\boldsymbol{\Delta\beta}_{SH-i}$ represents the isotropic part undetected by SV waves, that is, a portion of $\boldsymbol{\Delta\beta}_{SH}$ that exists in the model nullspace of the SV-velocity model (Chang *et al.* 2010). The other part, $\boldsymbol{\Delta\beta}_{SH-a}$, is the remaining minimal anisotropic structure. By definition, $\boldsymbol{\Delta\beta}_{SH-i}$ satisfy the following equation:

$$\mathbf{G}_{SV}\boldsymbol{\Delta\beta}_{SH-i} = 0, \tag{6}$$

where $\mathbf{G}_{SV}$ is SV sensitivity kernels used in Chang *et al.* (2010), because $\boldsymbol{\Delta\beta}_{SH-i}$ is in the model nullspace from $\mathbf{G}_{SV}$. To obtain $\boldsymbol{\Delta\beta}_{SH-i}$ and $\boldsymbol{\Delta\beta}_{SH-a}$, we invert the following equation:

$$\mathbf{G}_{SV}\boldsymbol{\Delta\beta}_{SH} = \mathbf{G}_{SV}(\boldsymbol{\Delta\beta}_{SH-i} + \boldsymbol{\Delta\beta}_{SH-a}) = \mathbf{G}_{SV}\boldsymbol{\Delta\beta}_{SH-a} = \mathbf{d}_{SVH}. \tag{7}$$

We already have the sensitivity kernel, $\mathbf{G}_{SV}$, and we can calculate the virtual data vector, $\mathbf{d}_{SVH}$, by multiplying $\mathbf{G}_{SV}$ with $\boldsymbol{\Delta\beta}_{SH}$. The same regularization and weighting factors in the resolution tests aforementioned are applied to this inversion to get $\boldsymbol{\Delta\beta}_{SH-a}$.

The inversion results of $\boldsymbol{\Delta\beta}_{SH-i}$ and $\boldsymbol{\Delta\beta}_{SH-a}$ are shown in Figs 5(b) and 6(a), respectively, at various depths. The isotropic part, $\boldsymbol{\Delta\beta}_{SH-i}$, does not have a significant amplitude and the remaining anisotropic model $\boldsymbol{\Delta\beta}_{SH-a}$ is 65 per cent correlated with and smoother than the anisotropic model $\boldsymbol{\Delta\beta}_{SH}$ (Fig. 5a).

5 RESULTS AND DISCUSSION

Results for radial anisotropy are shown at various depths along with the 3-D reference SV-velocity model in Fig. 6. Compared to 1-D model MEAN, this 3-D SV-velocity model (Fig. 6b) explains 87 per cent of the regional SV waveform variance (Chang *et al.* 2010), 72 per cent of the Rayleigh wave group velocity variance (Chang *et al.* 2010), 28 per cent of the regional SH waveform variance and 38 per cent of the Love-wave group velocity variance. The final SH-velocity model (Fig. 6a) explains an additional 60 per cent of the regional SH waveform variance and an additional 16 per cent of the Love-wave group velocity variance. General trends in our results are consistent with those found by Marone *et al.* (2004a) for the Mediterranean region.

5.1 Depth dependence of radial anisotropy

Babuška *et al.* (1998) observed depth dependence of radial anisotropy at different tectonic environments using data from the anisotropic upper mantle model by Montagner & Tanimoto (1991). They categorized the depth dependence of radial anisotropy perturbed from the reference anisotropy model, ACY400 (Montagner & Anderson 1989), into roughly three groups. First, SH velocity is faster than SV velocity beneath Phanerozoic orogenic belts with two

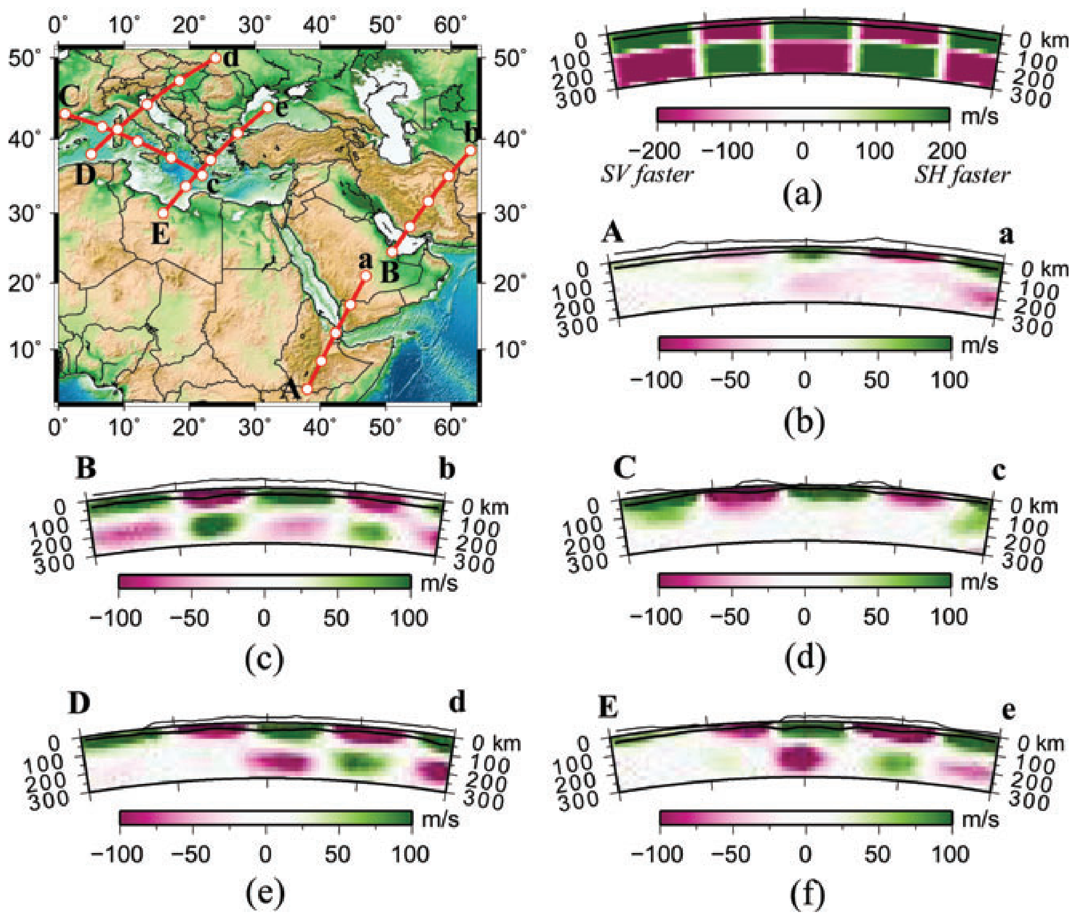

Figure 4. Checkerboard tests for vertical cross-sections. Vertical cross-sections are presented for (a) the true model, (b) beneath Afar, (c) beneath the Zagros belt and the Lut block, (d) from the Algero-Provençal basin to around Crete, (e) beneath the northern Apennines and the Pannonian basin and (f) perpendicular to the Hellenic arc. Moho depth and surface topography are shown in black solid lines. Topography is exaggerated 10 times. Great-circle paths corresponding to cross-sections are indicated on the left-top map. White circles on the great-circle paths correspond to ticks shown in the cross-sections.

peaks around 75 and 250 km depth. Second, *SH* velocity is faster than *SV* velocity beneath oceans shows a peak at ∼70 km depth and reaches down to ∼200 km depth. Third, faster *SV* velocity is observed down to 150–200 km depth in cratons.

Our results (Fig. 6a) generally coincide with Babuška *et al.*'s, with some exceptions. Faster *SH* velocity is accordingly observed down to 250 km depth beneath orogenic belts such as the Alps, the Dinarides and the Caucasus, which corresponds to the first group of Babuška *et al.* (1998), but we cannot resolve whether the faster *SH* velocity around 250 km is a peak or not. Silver (1996) suggested that faster *SH* velocity beneath the Phanerozoic orogenic belts may be caused by frozen-in fossil anisotropy formed by transpressional deformation during continental collision.

Faster *SH* velocity which corresponds to the second group of Babuška *et al.* is found beneath the Ionian Sea down to around 100–150 km depth with a peak amplitude a depth of 75 km. This is typical radial anisotropy of oceanic lithosphere in Babuška *et al.*'s categories, and is supported by Marone *et al.* (2004b) and Chang *et al.* (2010) who confirmed the origin of this region to be oceanic lithosphere, because of its thin crust and relatively high-velocity lithosphere. This radial anisotropy may be caused by olivine LPO frozen in the lithosphere and current horizontal flow in the asthenosphere.

Our results also show faster *SV* velocity in cratons such as the East European platform and the Arabian shield. Faster *SV* velocity in stable craton such as the East European platform may be attributed to the remnant fabric of palaeosubduction from past oceanic lithosphere. However, faster *SV* velocity within the Arabian shield may be caused by buoyancy-driven, vertical strain, because this region has experienced rifting since the Miocene, causing high topography (Almond 1986; Bohannon *et al.* 1989). On the other hand, beneath the Arabian platform *SH* velocity is faster than *SV* velocity. This lateral change in radial anisotropy beneath the Arabian Peninsula is similar to that found by Tkalčić *et al.* (2006). Faster *SV* velocity is also observed beneath the Algero-Provençal basin, Afar and the Lut block in Iran, and we discuss these anomalies below. Faster *SV* velocity beneath North Africa is not interpreted due to limited resolution (Fig. 3).

5.2 Radial anisotropy beneath hotspots

Beneath Afar, faster *SV* velocity is detected down to about 120 km depth, and then faster *SH* velocity is juxtaposed with weak amplitude below 120 km depth (Fig. 7a). This juxtaposition horizontally extends to about 1000 km. This anisotropy distribution with different polarity beneath Afar corresponds to a large low *SV*-velocity anomaly thought to be caused by the Afar mantle plume. Despite diminished resolving power on line A-a (Fig. 4b), resolution tests show that boundary of polarity change beneath Afar can be resolved

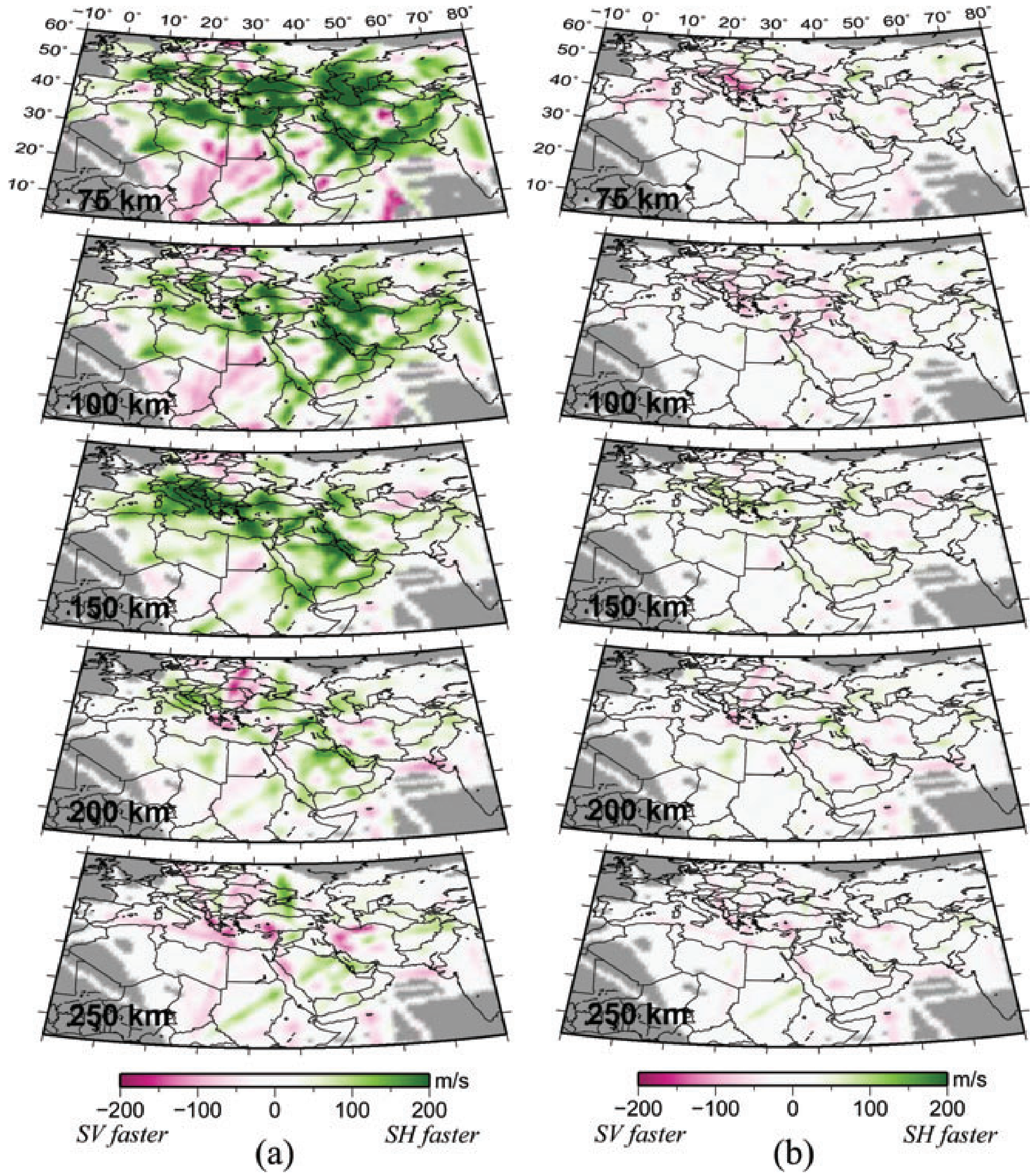

Figure 5. Inversion results of radial anisotropy and the isotropic part in the inversion results are presented at 75, 100, 150, 200 and 250 km depth. (a) This part indicates the joint inversion results ($\boldsymbol{\Delta\beta}_{SH}$) obtained from the inversion in eq. (3). (b) This part represents isotropic structure in the inversion results ($\boldsymbol{\Delta\beta}_{SH-i}$) obtained from eqs (5)–(7).

by our data. Moreover, Sicilia *et al.* (2008) also observed this boundary at around 120–150 km depth from their simultaneous inversion of *S* velocity and anisotropy with good surface wave coverage for Afar. A similar anisotropic feature was reported beneath a region near Iceland with a boundary at around 100 km depth (Gaherty 2001).

Karato *et al.* (2008) considered different types of olivine LPO associated with the same direction of mantle flow to explain this polarity change of radial anisotropy. If the deep mantle plume contains several times more water than in the asthenosphere, the olivine LPO in the mantle plume is likely to be C-type characterized by the [001] axis subparallel to the shear direction and the (100) plane subparallel to the shear plane. For C-type olivine LPO, *SV* velocity is faster than *SH* velocity for horizontal flow and *SH* velocity is weakly faster than *SV* velocity for vertical flow. Thus, fast *SH* velocity below ∼120 km would actually represent vertical mantle flow there. Because of assumed water contents and high temperature (100–200 K over typical temperature) in mantle plumes, dehydration by partial melt occurs relatively deep (∼100–200 km). Dry A-type with the [100](010) slip system or E-type with the [100](001) slip system thus form if all partial melt is migrated to the surface without any interaction with nearby materials. The effect of A- or E-type olivine LPO on radial anisotropy is opposite to that of C-type olivine LPO on radial anisotropy, so the fast *SV* velocity above ∼120 km would indicate vertical mantle flow. In conclusion, the polarity change of radial anisotropy at ∼120 km depth could represent a dehydration front of the upwelling plume material and a transition from C-type fabric below the front to A or E-type above the front, indicating consistent vertical mantle flow through the whole upper mantle beneath Afar.

However, Karato *et al.*'s argument is possible only if the deep mantle plume contains several times more water than in the

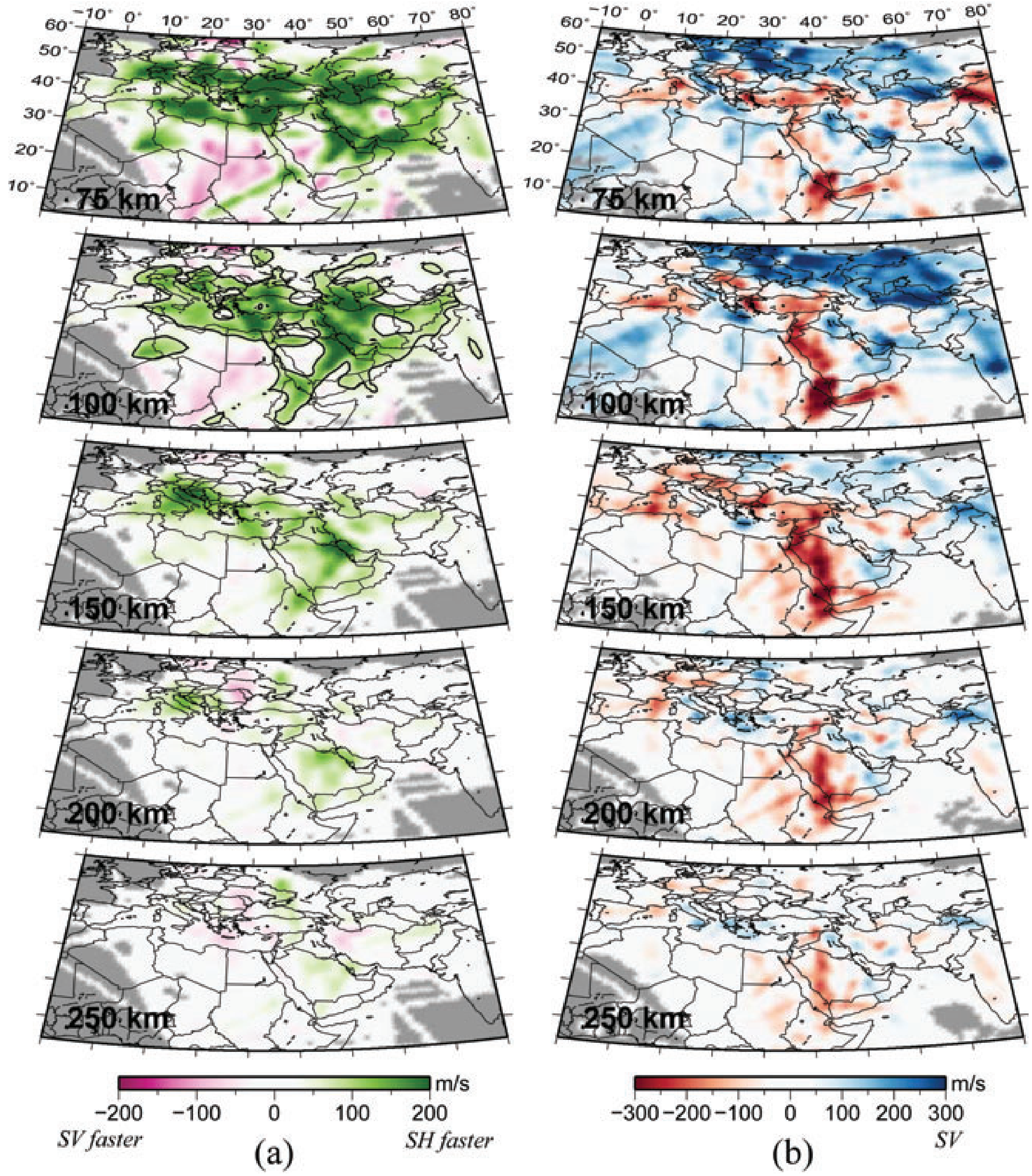

Figure 6. Anisotropic structure ($\Delta\beta_{SH-a}$) (a) obtained from the inversion results with eqs (5)–(7) at 75, 100, 150, 200 and 250 km depth are presented with the reference *SV*-velocity model (b). Contours of 66 m s^{-1} are drawn at 100 km depth in the anisotropic model. Regions not covered by data set are in grey.

asthenosphere and all partial melt is migrated to the surface without any interaction with nearby materials. We alternatively propose a hypothesis with 'relatively dry' mantle plume, which would contain A- or E-type olivine LPO. In this case, a change of radial anisotropy simply indicates a change in the direction of mantle flow: faster *SH* velocity would mean horizontal flow, while faster *SV* velocity would indicate vertical flow. Therefore, the transition at ∼120 km depth would approximately correspond to a lithosphere-asthenosphere boundary (LAB) and may represent a boundary between A or E-type LPO from horizontal deformation of plumehead in the asthenosphere to shape-preferred orientation (SPO) due to vertically oriented melt channels in the lithosphere. The vertical melt channels may connect low-velocity anomalies in the asthenosphere beneath Afar (Fig. 7a) with volcanism spread over the surface since about 30 Ma (Camp & Roobol, 1992). The boundary depth of ∼120 km is similar to the estimated LAB of 100–110 km by Rychert & Shearer (2009) using *Ps* converted phases, implying a relationship between the boundary of polarity change and LAB. The maximum amplitude of radial anisotropy in the lithosphere beneath Afar is about 250 m s^{-1} of faster *SV* velocity, which is about one third of the anisotropy inferred for *S* wave travelling through a region with a 10 per cent density of aligned cracks or films (Kendall, 1994). Webb and Forsyth (1998) also document the dramatic effect of as little as 1 per cent melt aligned in thin films on *S* velocity (up to 40 per cent change).

We also observe a similar juxtaposition of faster *SV* and *SH* velocities at around 120 km depth for a wide area beneath the Lut block (Fig. 7b), which may imply that there is a transition from LPO due to horizontal flow in the asthenosphere to SPO from vertical melt channels in the lithoshpere based on our hypothesis. This observation may support the existence of a mantle plume here, which Chang *et al.* (2010) proposed based on a plume-like

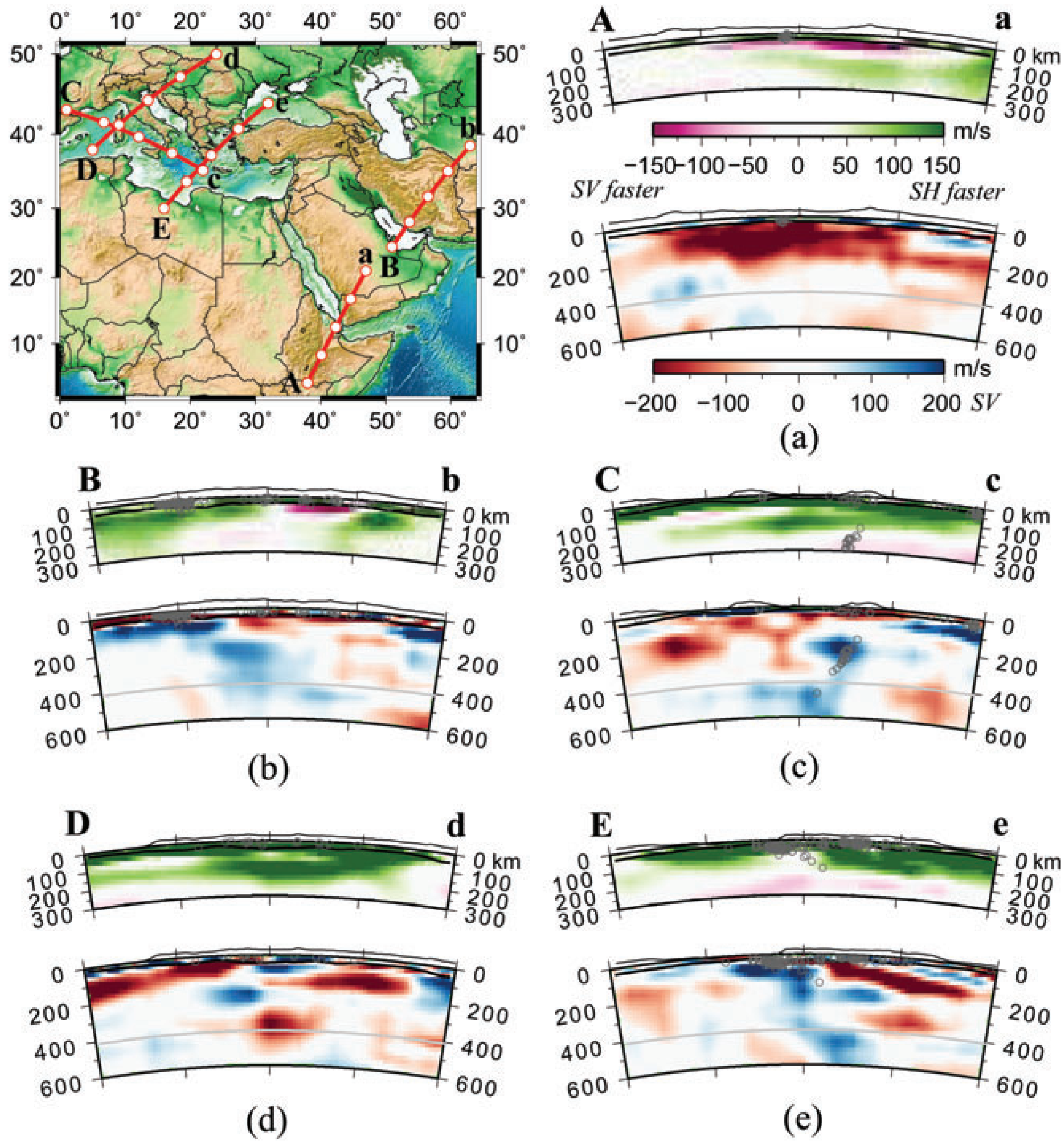

Figure 7. Vertical cross-section maps of radial anisotropy ($\Delta\beta_{SH-a}$) and the reference *SV*-velocity model profiles beneath Afar (a), beneath the Zagros belt and the Lut block (b), from the Algero-Provençal basin to around Crete (c), beneath the northern Apennines and the Pannonian basin (d) and perpendicular to the Hellenic arc (e). Cross-sections of radial anisotropy are presented on the top and ones of the *SV*-velocity model are illustrated on the bottom. The same scales as in (a) are applied to (b)–(e). Moho depth and surface topography are shown in black solid lines. Moho depth distribution is adopted from Chang *et al.* (2010). Topography is exaggerated 10 times. Grey open circles represent events. Regions not covered by data sets are in grey. Great-circle paths corresponding to cross-sections are indicated on the left-top map. White circles on the great-circle paths correspond to ticks shown in the cross-sections.

low-velocity anomaly imaged in the *SV*-velocity model down to at least the mantle transition zone. Conclusively, the juxtaposition of faster *SV* and *SH* velocities are observed beneath Iceland, Afar and the Lut block which are known as or thought to be regions intruded by mantle plumes, so this peculiar feature of radial anisotropy may be typical to mantle plumes.

5.3 Radial anisotropy beneath backarc basins

Cross-sections of radial anisotropy beneath backarc basins, the Algero-Provençal and the Tyrrhenian basins in the western Mediterranean Sea and the Pannonian basin near the Carpathians, are presented in Figs 7(c) and (d). The characteristics of anisotropy for backarc basins are quite different from those for the hotspots. The backarc basin mantle is dominated by faster *SH* velocity, which may represent dominant horizontal flow beneath the backarc basins.

However, features of radial anisotropy are a little different between the two backarc basins in the western Mediterranean Sea. Although *SH* velocity is dominantly faster than *SV* velocity beneath the Tyrrhenian basin, anisotropy underneath the Algero-Provençal basin shows that *SV* velocity is faster than *SH* velocity for 80–120 km depth.

This difference may be caused by different tectonic processes for the two basins. As the Calabrian slab which began to subduct about 35 Ma ago has retreated to the current position, mantle flow pushed by the slab roll back has moved to the backarc region to fill the space left behind the retreating slab. Because the slab did not reach to the transition zone when the Algero-Provençal basin opened, the mantle flow moved below the slab's tip (Lucente *et al.* 2006). Therefore, the observed faster *SV* velocity beneath Algero-Provençal basin may be the preserved vertical mantle flow since the opening of the basin. In the other hand, when the Tyrrhenian basin opened, mantle flow could not move below the slab's tip, because the flattened slab within the mantle transition zone hampered the movement of mantle flow below the slab. Instead, formation of the Tyrrhenian basin may be achieved by horizontal mantle flow through slab windows beneath central Italy and west of Sicily (Lucente *et al.* 2006; Lucente & Margheriti 2008), which has resulted in faster *SH* velocity beneath this basin.

5.4 Anisotropy around subduction zones

Much of the world's most intricate anisotropy occurs in subduction zones. Compilations and studies of subduction zone anisotropy have generally focused on splitting of near-vertically travelling shear waves (e.g. Russo & Silver 1994; Kaneshima & Silver 1995; Fischer *et al.* 1998; Long & Silver, 2008), which are most sensitive to azimuthal anisotropy related to horizontal mantle flow in the backarc or subslab mantle but less to radial anisotropy within the dipping slab itself.

Using the depth resolution of surface waves and our dense wave path coverage (Fig. 4), we estimated radial anisotropy also within dipping slabs. Within our study area, major subducting slabs are found beneath the Apennines, the Calabrian arc, the Hellenic arc and the Zagros belt. The distribution of radial anisotropy for these subducting slabs is shown in Fig. 7. Beneath the Calabrian arc (Fig. 7c), high *SV*-velocity anomalies are aligned with the event distribution in the bottom panel indicating the location of the Calabrian slab, which corresponds to faster *SV* velocity below 150–200 km in the middle panel. Faster *SV* velocity is also detected at 150–200+ km beneath regions where steeply dipping slabs exist such as the Zagros belt and the Hellenic arc in Figs 7(b) and (e). However, at shallower depths than 150–200 km where the slabs are dipping gently, faster *SH* velocity is observed (Figs 7b,c and e) as in radial anisotropy of oceanic lithosphere by Babuška *et al.* (1998). Within the Apenninic slab which has gentle dipping down to about 300 km depth faster *SH* velocity is also observed (Fig. 7d).

This dependence of radial anisotropy on the dip of slab may indicate that frozen-in fossil anisotropy with faster *SH* velocity in oceanic lithosphere is preserved to considerable depth in the upper mantle after subduction, which is consistent with experiments with dipping olivine by Maupin & Park (2007). This dependence also can be explained by serpentine deformation in the mantle wedge (Katayama *et al.* 2009), because the fast a axis of serpentine aligns along the slab.

5.5 Strength of anisotropy

Our results (Figs 6 and 7) show that our study region is dominated by faster *SH* velocity than *SV* velocity ($\beta_{SH} > \beta_{SV}$). The region where $\beta_{SH} - \beta_{SV} > 66$ m s^{-1} (1.5 per cent) is outlined in black on the 100-km depth map (Fig. 6a). The depth dependence of the average anisotropy within this region is plotted in Fig. 8, along with PREM (Dziewoński & Anderson 1981), which shows that there is remarkable agreement between the radial anisotropy in this region and PREM.

6 CONCLUSIONS

We estimated radial anisotropy beneath the Tethyan margin by jointly inverting regional *S* and Love waveform trains and fundamental Love-wave group velocities relative to the 3-D *SV*-velocity model by Chang *et al.* (2010). Faster *SV* velocity is generally detected in cratons such as the East European platform and the Arabian shield, while faster *SH* velocity is found beneath oceans and orogenic belts such as the Ionian Sea, the Alps, the Apennines, the Dinarides and the Caucasus. These features are generally consistent with Babuška *et al.* (1998)'s analysis and we have discussed the possible causes for the anisotropy in each of these tectonic environments.

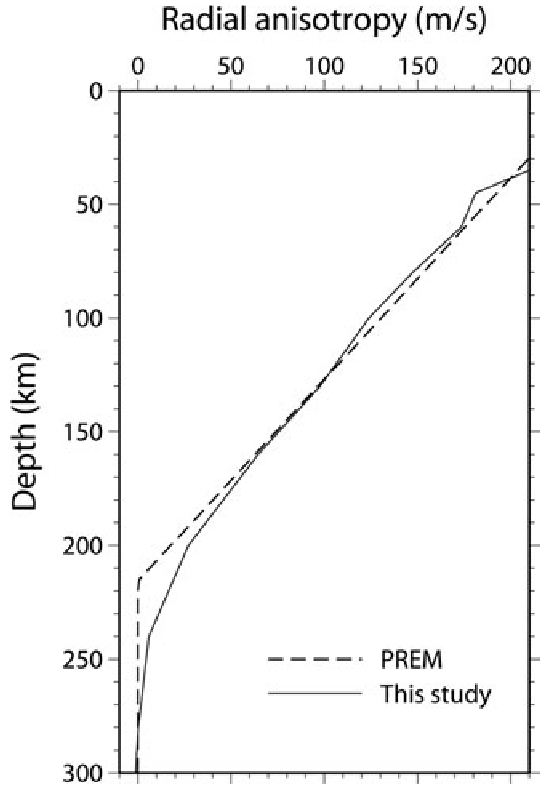

Figure 8. Average 1-D anisotropic structures. Anisotropic models from PREM (Dziewoński & Anderson 1981) and our study are shown in dashed and solid lines, respectively. The area considered in our study is defined by radial anisotropy >66 m s^{-1} (1.5 per cent of the reference model MEAN) at 100 km depth shown in Fig. 6a.

A change of the polarity of radial anisotropy with depth is found for wide low-velocity areas beneath Afar and the Lut block in Iran. This feature may indicate the lithosphere-asthenosphere boundary, where transition occurs between LPO from horizontal deformation of plumehead in the asthenosphere and SPO from vertical melt channels in the lithosphere.

The two backarc basins in the western Mediterranean Sea exhibit different patterns of anisotropic features: faster *SV* and *SH* velocity beneath the Algero-Provençal and Tyrrhenian basins, respectively. This difference in radial anisotropy may indicate different tectonic environments for each basin, because the opening of the Algero-Provençal basin may have been caused by vertical mantle flow travelling below slab's tip while the opening of the Tyrrhenian basin may have been complete by horizontal flow through slab windows (Lucente *et al.* 2006).

Finally, we infer that anisotropy within oceanic lithosphere can be preserved to considerable depth during subduction. Near the surface, where the slab is still predominantly subhorizontal, we find typical faster *SH* velocity, down to about 150–200 km. Deeper, where slabs dip more steeply such as under the Calabrian arc, the

Hellenic arc and the Zagros belt, the same anisotropy now manifests itself as faster *SV* velocity.

ACKNOWLEDGMENTS

We thank Megan Flanagan, Federica Marone and Michael Pasyanos for sharing their waveform fit and group velocity data sets. We also thank an anonymous reviewer and Mark Panning for their valuable comments, which improved this manuscript. All figures were created using Generic Mapping Tools (GMT; Wessel & Smith 1998). This work was supported by the Korea Research Foundation Grant KRF-2006-214-C00092 funded by the Korean Government (MOEHRD) and the U.S. DOE under contract DE-FC52-04NA25541.

REFERENCES

Almond, D.C., 1986. Geological evolution of the Afro-Arabian dome, *Tectonophysics,* **131,** 301–322.

Babuška, V., Montagner, J.-P., Plomerová, J. & Girardin, N., 1998. Age-dependent large-scale fabric of the mantle lithosphere as derived from surface-wave velocity anisotropy, *Pure appl. Geophys.,* **151,** 257–280.

Bamford, D., 1973. Refraction data in western Germany—a time-term interpretation, *Z. Geophys.,* **39,** 907–927.

Bamford, D., 1977. Pn velocity anisotropy in a continental upper mantle, *Geophys. J. R. astr. Soc.,* **49,** 29–48.

Bassin, C., Laske, G. & Masters, G., 2000. The current limits of resolution for surface wave tomography in North America, *EOS, Trans. Am. geophys. Un.,* **81,** F897.

Baumgardner, R.B. & Frederickson, P.O., 1985. Icosahedral discretization of the two-sphere, *SIAM J. Numer. Anal.,* **22,** 1107–1115.

Bird, P., 2003. An updated digital model of plate boundaries, *Geochem. Geophys. Geosyst.,* **4,** 1027, doi:10.1029/2001GC000252.

Bohannon, R.G., Naeser, C.W., Schmidt, D.L. & Zimmermann, R.A., 1989. The timing of uplift, volcanism and rifting peripheral to the Red Sea: a case for passive rifting? *J. geophys. Res.,* **94,** 1683–1701.

Bozdağ, E. & Trampert, J., 2008. On crustal corrections in surface wave tomography, *Geophys. J. Int.,* **172,** 1066–1082.

Camp, V.E. & Roobol, M.J., 1992. Upwelling asthenosphere beneath western Arabia and its regional implications, *J. geophys. Res.,* **97,** 15 255–15 271.

Chang, S.-J., *et al*. 2010. Joint inversion for 3-dimenstional S-velocity mantle structure along the Tethyan margin, *J. geophys. Res.,* in press.

Constable, S.C., Parker, R.L. & Constable, C.G., 1987. Occam's inversion: a practical algorithm for generating smooth models from electromagnetic sounding data, *Geophysics,* **52,** 289–300.

Dziewoński, A.M. & Anderson, D.L., 1981. Preliminary reference Earth model, *Phys. Earth planet. Int.,* **25,** 297–356.

Ekström, G. & Dziewoński, A.M., 1998. The unique anisotropy of the Pacific upper mantle, *Nature,* **394,** 168–172.

Estey, L.H. & Douglas, B.J., 1986. Upper mantle anisotropy: a preliminary model, *J. geophys. Res.,* **91,** 11 393–11 406.

Fischer, K.M., Fouch, M.J., Wiens, D.A. & Boettcher, M.S., 1998. Anisotropy and flow in Pacific subduction zone back-arcs, *Pure appl. Geophys.,* **151,** 463–475.

Gaherty, J.B., 2001. Seismic evidence for hotspot-induced buoyant flow beneath the Reykjanes ridge, *Science,* **293,** 1645–1647.

Gung, Y., Panning, M. & Romanowicz, B., 2003. Global anisotropy and the thickness of continents, *Nature,* **422,** 707–711.

Hess, H.H., 1964. Seismic anisotropy of the uppermost mantle under oceans, *Nature,* **203,** 629–631.

Kaneshima, S. & Silver, P.G., 1995. Anisotropic loci in the mantle beneath central Peru, *Phys. Earth planet. Inter.,* **88,** 257–272.

Karato, S., Jung, H., Katayama, I. & Skemer, P., 2008. Geodynamic significance of seismic anisotropy of the upper mantle: new insights from laboratory studies, *Annu. Rev. Earth planet. Sci.,* **36,** 59–95.

Katayama, I., Hirauchi, K., Michibayashi, K. & Ando, J., 2009. Trench-parallel anisotropy produced by serpentine deformation in the hypdrated mantle wedge, *Nature,* **461,** 1114–1118.

Kendall, J.-M., 1994. Teleseismic arrivals at a mid-ocean ridge: effects of mantle melt and anisotropy, *Geophys. Res. Lett.,* **21,** 301–304.

Long, M.D. & Silver, P.G., 2008. The subduction zone flow field from seismic anisotropy: a global view, *Science,* **319,** 315–318.

Lucente, F.P. & Margheriti, L., 2008. Subduction rollback, slab breakoff, and induced strain in the uppermost mantle beneath Italy, *Geology,* **36,** 375–378, doi:10.1130/G24529A.

Lucente, F.P., Margheriti, L., Piromallo, C. & Barruol, G., 2006. Seismic anisotropy reveals the long route of the slab through the western-central Mediterranean mantle, *Earth planet. Sci. Lett.,* **241,** 517–529.

Marone, F. & Romanowicz, B., 2007. Non-linear crustal corrections in high-resolution regional waveform seismic tomography, *Geophys. J. Int.,* **170,** 460–467.

Marone, F., Van Der Meijde, M., Van Der Lee, S. & Giardini, D., 2003. Joint inversion of local, regional and teleseismic data for crustal thickness in the Eurasia-Africa plate boundary region, *Geophys. J. Int.,* **154,** 499–514.

Marone, F., Van Der Lee, S. & Giardini, D., 2004a. Shallow anisotropy in the Mediterranean mantle from surface waves, *Geophys. Res. Lett.,* **31,** L06624, doi:10.1029/2003GL018948.

Marone, F., Van Der Lee, S. & Giardini, D., 2004b. Three-dimensional upper-mantle *S*-velocity model for the Eurasia-Africa plate boundary region, *Geophys. J. Int,* **158,** 109–130.

Marone, F., Gung, Y. & Romanowicz, B., 2007. Three-dimensional radial anisotropic structure of the North American upper mantle from inversion of surface wave data, *Geophys. J. Int.,* **171,** 206–222.

Maupin, V. & Park, J., 2007. Theory and observations—wave propagation in anisotropic media, in *Treatise on Geophysics,* Chapter 1.09, pp. 289–321, ed. Schubert, G., Elsevier, Amsterdam, doi:10.1016/B978-044452748-6/00007-9.

Montagner, J.-P. & Anderson, D.L., 1989. Constrained reference mantle model, *Phys. Earth planet. Int.,* **58,** 205–227.

Montagner, J.-P. & Tanimoto, T., 1991. Global upper mantle tomography of seismic velocities and anisotropies, *J. geophys. Res.,* **96,** 20 337–20 351.

Nolet, G., 1990. Partitioned waveform inversion and 2-dimensional structure under the network of autonomously recording seismographs, *J. geophys. Res.,* **95,** 8499–8512.

Paige, C.C. & Saunders, M.A., 1982a. LSQR: an algorithm for sparse linear equations and sparse least squres, *ACM Trans. Math. Softw.,* **8,** 43–71.

Paige, C.C. & Saunders, M.A., 1982b. LSQR: sparse linear equations and least squares problems, *ACM Trans. Math. Softw.,* **8,** 195–209.

Panning, M. & Romanowicz, B., 2006. A three-dimensional radially anisotropic model of shear velocity in the whole mantle, *Geophys. J. Int.,* **167,** 361–379.

Pasyanos, M.E. & Nyblade, A.A., 2007. A top to bottom lithospheric study of Africa and Arabia, *Tectonophysics,* **444,** 27–44.

Plomerová, J., Kouba, D. & Babuška, V., 2002. Mapping the lithosphere-asthenosphere boundary through changes in surface-wave anisotropy, *Tectonophysics,* **358,** 175–185.

Russo, R.M. & Silver, P.G., 1994. Trench-parallel flow beneath the Nazca plate from seismic anisotropy, *Science,* **263,** 1105–1111.

Rychert, C.A. & Shearer, P.M., 2009. A global view of the lithosphere-asthenosphere boundary, *Science,* **324,** 495–498.

Savage, M.K., 1999. Seismic anisotropy and mantle deformation: what have we learned from shear wave splitting?, *Rev. Geophys.,* **37,** 65–106.

Schmid, C., Van Der Lee, S. & Giardini, D., 2004. Delay times and shear wave splitting in the Mediterranean region, *Geophys. J. Int.,* **159,** 275–290.

Sebai, A., Stutzmann, E., Montagner, J.-P., Sicilia, D. & Beucler, E., 2006. Anisotropic structure of the African upper mantle from Rayleigh and Love wave tomography, *Phys. Earth planet. Inter.,* **155,** 48–62.

Sicilia, D. *et al*. 2008. Upper mantle structure of shear-waves velocities and stratification of anisotropy in the Afar Hotspot region, *Tectonophysics,* **462,** 164–177.

Silver, P.G., 1996. Seismic anisotropy beneath the continents: probing the depths of geology, *Annu. Rev. Earth planet. Sci.,* **24,** 385–432.

Silver, P.G. & Chan, W.W., 1991. Shear wave splitting and subcontinental mantle deformation, *J. geophys. Res.,* **96,** 16 429–16 454.

Tkalčić, H., Pasyanos, M.E., Rodgers, A.J., Gök, R., Walter, W.R. & Al-Amri, A., 2006. A multistep approach for joint modeling of surface wave dispersion and teleseismic receiver functions: implications for lithospheric structure of the Arabian Peninsula, *J. geophys. Res.,* **111,** B11311, doi:10.1029/2005JB004130.

Van Der Lee, S. & Nolet, G., 1997. Upper mantle *S* velocity structure of North America, *J. geophys. Res.,* **102,** 22 815–22 838.

VanDecar, J.C., 1991. Upper-mantle structure of the Cascadia subduction zone from non-linear teleseismic travel-time inversion, *Ph.D. thesis*. University of Washington, Seattle.

Wang, Z. & Dahlen, F.A., 1995. Spherical-spline parameterization of three-dimensional Earth models, *Geophys. Res. Lett.,* **22,** 3099–3102.

Webb, S.C. & Forsyth, D.W., 1998. Structure of the upper mantle under the EPR from waveform inversion of regional events, *Science,* **280,** 1227–1229.

Wessel, P. & Smith, W.H.F., 1998. New, improved version of the Generic Mapping Tools released, *EOS, Trans. Am. geophys. Un.,* **79,** 579.